Hydrological issues in lateral boundary conditions for regional climate modeling: simulation of east asian summer monsoon in 1998

Bin Wang · Hongwei Yang

Abstract The atmospheric branch of the hydrological cycle associated with the East Asian summer monsoon is intricate due to its distinct land-sea configurations: the highest mountains are to its west, the oceans are to its south and east, and mid-latitude influences come from its north. Here we use the weather research and forecast (WRF) model to demonstrate that using two different large-scale driving fields, derived from the NCEP/DOE R2 and ERA40 reanalysis data and the same model configuration yielded remarkable differences. We found that the differences are primarily caused by uncertainties in the water vapor influx across the lateral boundaries in the reanalyses. The summer-mean water vapor convergence into the model domain computed from the ERA40 reanalysis is 47% higher than that from the R2 reanalysis. The largest uncertainties in moisture transport are found in the regions of the Philippine Sea and the Bay of Bengal, where the moisture transport has the most significant impacts on the East Asian summer monsoon rainfall distribution. The sensitivity test results suggest that the biases in the seasonal mean, seasonal march of the rain band, and individual rainfall events may be reduced by using an "ensemble" average of R2 and ERA40 as lateral boundary forcing. While the large-scale forcing field does not conserve water vapor, the WRF simulation conserves water vapor in the inner model domain. The regional model simulation has corrected the biases in the total amount and the month-to-month distribution of precipitation in the large-scale driving field. However, RCM's daily precipitation is poorer than that in the reanalysis filed. Since the RCM solutions may sensitively depend on the reanalysis forcing, inter-comparison of models' performance based on a single set of the reanalysis may not be reliable. This calls for attention to reshape our strategy for validation of RCMs.

B. Wang (✉) · H. Yang
International Pacific Research Center and
Department of Meteorology,
School of Ocean and Earth Science and Technology,
University of Hawaii, Honolulu, HI 96822, USA
e-mail: wangbin@hawaii.edu

H. Yang
LASG, Institute of Atmospheric Physics,
Chinese Academy of Sciences, Beijing, China

B. Wang
College of Physical Oceanography and Environment,
Ocean University of China, 266100 Qingdao, China

1 Introduction

The field of regional climate modeling is booming due to enormous demands for prediction of future regional climate change, downscaling seasonal predictions, and for use in a variety of regional climate applications. It is, therefore, imperative to better understand the strengths, deficiencies, and limitations as well as the sources of uncertainties that can occur with regional climate model (RCM) simulations. A number of RCM intercomparison projects have been carried out to identify common model strengths and weaknesses over specific regions such as Europe (Christensen et al. 1997), the United States of America (Takle et al. 1999; Curry and Lynch 2002; Anderson et al. 2003), and East Asia (Leung and Ghan 1999; Fu et al. 2005).

To a large extent, a RCM simulation that is nested in a global environment presents a boundary value problem. The sensitivity of the RCM to the large-scale lateral boundary (LB) forcing has been well recognized (e.g., Miyakoda and Rosati 1977; Jacob and Podzun 1997;

Paegle et al. 1997; Giorgi and Bi 2000; Liang et al. 2001, 2004; Pan et al. 2001; Wu et al. 2005; Zhong 2006). Some studies focused on the impacts of domain sizes (Jones et al. 1995; Bhaskaran et al. 1996; Liang et al. 2001) and consistency between the driving GCM and driven RCM (Beniston et al. 2007). The Big-Brother experiment (Denis et al. 2002) shows that one-way nesting strategy has skills in downscaling large-scale information to the regional scales.

However, determining the way in which the uncertainties in the LB conditions affect RCM solutions has been inconclusive. Some studies have reported that the RCMs were unable to lessen the errors in large-scale forcing fields (Vukicevic and Errico 1990); on some occasions, the global models' errors tend to be amplified (Christensen et al. 1997). Other studies, in contrast, have found that the RCM is able to correct large-scale errors (e.g., Hong and Leetmaa 1999). The mixture of errors that arise from large-scale forcing and from model parameterizations adds complexity to the validation of the RCMs' performance and to the understanding of how the errors that are caused by the LB forcing are generated in the RCMs.

In simulations of the 1998 East Asian summer monsoon (EASM), successful simulation using a regional climate model (iRCM) was reported (Wang et al. 2003). It was noticed, however, that good simulation was obtained only when the European centre for Medium-Range Weather Forecasts 40-year reanalysis (ERA40) dataset was used as the LB forcing. Use of the National Centres for Environmental Prediction/National Centre for Atmospheric Research reanalysis product as LB forcing significantly degraded the simulation results. The root cause of the sensitivity of the model solution to the LB forcing in the reanalysis was not addressed. It was also not determined whether the sensitivity depends on the specific model that was used. In this study, we are motivated to use another RCM and use both ERA40 data and reanalysis 2 (R2) data from the National Centers for Environmental Prediction/ Department of Energy (NCEP/DOE) as driving forces to investigate why the simulation of the EASM is so sensitive to the large-scale LB conditions and to determine how the errors induced by the uncertainties in the LB conditions can be reduced.

Moisture and energy balances are fundamental to regional climate modeling and downscaling. Regional modeling of the EASM is a particular challenge because this region has the highest mountains on Earth, it faces the tropical Indian Ocean to the south and the North Pacific to the east, and it is subject to additional influences from the middle to high latitudes. The moisture transport and hydrological cycle of the EASM is more complex than those of the Indian monsoon. The sources of water vapor variations for the Indian monsoon come primarily from the southern Indian Ocean (Krishnamurti and Bhalme 1976; Fasullo and Webster 2002), whereas the sources of water vapor variations in the EASM come from the northern Indian Ocean, the South China Sea (including the cross-equatorial transport from the Southern Hemisphere), and the western North Pacific (e.g., Ding and Sikka 2006; Zhou and Yu 2005).

One of our concerns is the issue of moisture conservation in regional climate modeling. When a RCM is embedded in a global model, a buffer zone is often used between the lateral boundaries and the interior domain. Many fluid properties need to be constrained to make a smooth transition. However, we do not know how the moisture imbalance in the buffer zone influences the atmospheric hydrological cycle in the inner domain. When the reanalysis data are used as the LB forcing, a similar issue arises. The large-scale water vapor is not conserved in the reanalysis data. Given such forcing, will regional modeling improve the large-scale hydrological cycle?

The central questions to be addressed in this study are the following: How sensitive is the RCM solution to the large-scale boundary hydrological forcing in simulations of the EASM? How do the uncertainties in the large-scale thermal and circulation fields give rise to RCM errors? Can we reduce the impacts of those uncertainties to improve regional model simulations? Can a RCM correct precipitation biases in the large-scale driving field? To fully address these questions requires Decadal simulation (Jones et al. 1995). The present study is a pilot effort toward stimulating further investigations to attack these important issues.

The model and experimental design are described in the next section. Sections 3, 4, and 5 examine, respectively, the impacts and causes of the uncertainties in the LB forcing, the way to reduce the impact of uncertainties in the LB conditions, and the water vapor balance in regional climate modeling. The final section summarizes the major findings of this study.

## 2 The model and experimental design

2.1 The weather forecast and research (WRF) model and data

The weather forecast and research (WRF) model used in this study (version 2.0.31) adopts σ-coordinates and a top boundary at the pressure surface 50 hPa. The WRF model system offers multiple options for various physical packages (Skamarock et al. 2005). We used the following schemes: Lin cloud microphysics (Lin et al. 1983; Chen and Sun 2002), Betts–Miller–Janjic cumulus parameterization (Janjic 2000), Noah's land surface model (Chen and Dudhia 2001), Yongsei University planetary boundary-

layer parameterization (Noh et al. 2003), the rapid radiative transfer model for long-wave radiation, and the Dudhia (1989) scheme for the shortwave radiation. All model parameters were taken with the default values without tuning.

Two reanalysis datasets were used as the driving data: R2 (Kanamitsu et al. 2002) and ERA40 (Uppala et al. 2005). ERA40 is available at 6-h intervals on 17 pressure levels up to 10 hPa, with a horizontal resolution of 2.5° by 2.5° for both the pressure level and the surface data. R2 data are available at the same spatial and temporal resolution, except the surface data have a resolution of 1.85° by 1.85°. For the land surface model, the following datasets were used: topographic data with horizontal resolution of 30 seconds, the US Geological Survey (USGS) land-use data, and the 5-min soil type data from the Food and Agriculture Organization of the United Nations (UN/FAO).

To validate simulated precipitation fields, we used three datasets: the Global Precipitation Climatology Project (GPCP) daily precipitation with horizontal resolution of 1° by 1° (Huffman et al. 2001), the Climate Prediction Center (CPC) Merged Analysis of Precipitation (CMAP) monthly precipitation on 2.5° by 2.5° grids (Xie and Arkin 1997), and the observed daily precipitation data at 532 Chinese rain gauge stations, obtained from the Chinese National Meteorological Center. The locations of these rain gauge stations are shown in Fig. 1. In comparison with model simulation results, all observed precipitation data were interpolated into the model grids by using bilinear interpolation.
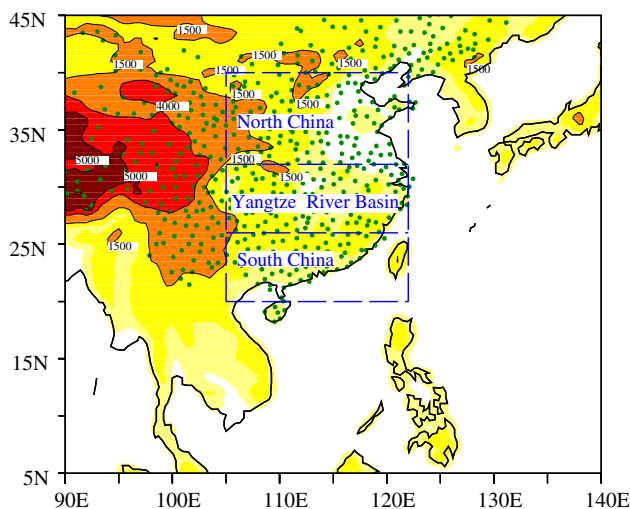
Fig. 1 Regional climate model (*RCM*) domain and topography (*color shading* in units of meters). Topographic contours of 1,500, 4,000 and 5,000 m are highlighted. The *solids* show the locations of 532 Chinese rain gauge stations. The *rectangular boxes* that were drawn by *dashed lines* refer to the following regions: South China (20°–26°N, 105°–122°E), the Yangtze River basin (26°–32°N, 105°–122°E), and North China (32°–40°N, 105°–122°E)

2.2 Experimental design

The case examined here is the 1998 rainy season in East Asia, during which severe flood occurred in the Yangtze River basin in June and July (Ding and Liu 2001). The experimental domain covers the area between 5° and 45°N and between 90° and 140°E. The Mercator map projection was adopted. The zonal grid space is precisely 0.5°, and the meridional grid space is approximately 0.5° with a slight northward decrease. The domain contains 92 (meridional) and 101 (zonal) grid points. Thirty-one σ levels in the vertical direction were chosen. Figure 1 shows the topography map. The steepest slope on Earth is located south and east of the Tibetan Plateau. Clay loam and regular loam are dominant soil types across East Asia. Grasslands and croplands occupy most of the area in the central China. Barren or sparsely vegetated land cover is located in the northwestern part of the domain. Forests are found in the northeastern part of the domain and in the southern flank of the Tibetan Plateau and Indochina.

To study the sensitivity of the model to the LB conditions, we initially designed two ensemble experiments, in which the R2 and ERA40 reanalysis data were used as initial and time-varying LB conditions. Each of the ensemble experiments has 5 members with different initial conditions spanning 5 days centered on 12Z April 24, 1998; for brevity, their ensemble mean are labeled Exp R2 and Exp ERA40, respectively. The forcing fields include air temperature, specific humidity, zonal and meridional winds, and geopotential height at standard pressure levels, which were interpolated to match the regional model resolution. The surface initial conditions include surface pressure, sea-level pressure, temperature and moisture at a 2-m height, skin temperature on the land surface, horizontal wind at a 10-m height, water equivalent of snow depth, soil moisture, and soil temperature. The skin temperatures over the ocean were considered sea surface temperature (SST). The days before May 1 were considered a "spin-up" period (Giorgi and Mearns 1999). The ensemble mean of the outputs from May 1 to August 31 were analyzed. The physical parameterizations and model configuration were kept the same for all experiments. All model parameters were taken with the default values without tuning.

3 Origins of the biases induced by the LB forcing

3.1 Biases induced by the LB forcing

With different LB conditions, the two sensitivity experiments yielded different systematic biases in their simulations of June–July–August (JJA) mean low-level

circulations. Figure 2a shows the observed mean 850 hPa height and horizontal winds during the summer (JJA). This field is derived by averaging the corresponding fields from the R2 and ERA40 data. Note that the corresponding fields that are derived from both R2 and ERA40 are so close to each other that their ensemble mean does not appreciably differ from each individual dataset. Figures 2b and c compare the biases in the 850 hPa circulations obtained from Exp R2 and Exp ERA40. The results from Exp ERA40 show remarkable biases (Fig. 2c): a major low-pressure and cyclonic bias is located over eastern China and the East China Sea board centered on Taiwan. The biases in Exp R2 are considerably smaller than those in Exp ERA40 but have opposite polarities: A weak anticyclonic and high-pressure bias is seen in eastern China and East China Sea board. The biases in the two experiments reflect large discrepancies in the model's simulations of the location and strength of the western North Pacific (WNP) subtropical high. This is a key weather system that determines the locations of the subtropical front and primary monsoon rain band in East Asia. Therefore, the biases have far-reaching consequences on the summer monsoon precipitation and circulation. The bias patterns tend to persist through each month of the summer, although they fluctuate from month to month (figure not shown).

Biases are not only seen in the monthly and seasonal mean fields, but also seen in the simulation of the seasonal march of the major monsoon precipitation band. Northward migration of the subtropical front and associated rain band is one of the prominent features of the EASM. To depict this seasonal march, we present in Fig. 3 the time-latitude cross-section along the longitudinal band between 105 and 122°E over eastern China (see Fig. 1 for the location of the longitude band). To validate the model precipitation, we used the Chinese rain gauge data over the land area (see Fig. 1 for the locations) with implementation of GPCP data over the sea and Taiwan. The observed time-latitude cross-section shows that the rain band migrates northward from 18°N in early June to 40°N in mid-July (Fig. 3a). The average speed of northward movement is approximately 0.5° latitude per day. This northward migration reflects the seasonal march of the EASM rain band (Wang and LinHo 2002). It is noteworthy that the simulation with ERA40 as LB forcing fails to capture the northward journey of the rain band (Fig. 3d). The map correlation coefficient between the observation (Fig. 3a) and ERA40 run (Fig. 3d) is only 0.33. Compared to Exp ERA40, the Exp R2 simulation shows better agreement with the observed northward march, but it is still far from realistic (Fig. 3b). The results here suggest that large discrepancies in Exp R2 and Exp ERA40 are not only seen in the seasonal mean fields but also in the seasonal evolutions.

Fig. 2 **a** Summer June–July–August (*JJA*) mean geopotential height (*shading* in units of metre) and horizontal winds (*vector* in units of ms^{-1}) at 850 hPa that are derived from the ensemble mean of R2 and ERA40 reanalysis data. Shown in (**b**), (**c**) and (**d**) are the WRF model biases that were simulated with lateral boundary (*LB*) conditions derived from (**b**) NCEP/DOE reanalysis 2 (*R2*), **c** ECMWF reanalysis (*ERA40*), and **d** ensemble mean of ERA40 and R2 control (*CTL*), respectively. All the biases are defined by the departure of RCM simulations from the ensemble mean of R2 and ERA40. The *purple circles* indicate the significant areas with 99% confidence level in the difference of *geopotential height* by *t* test
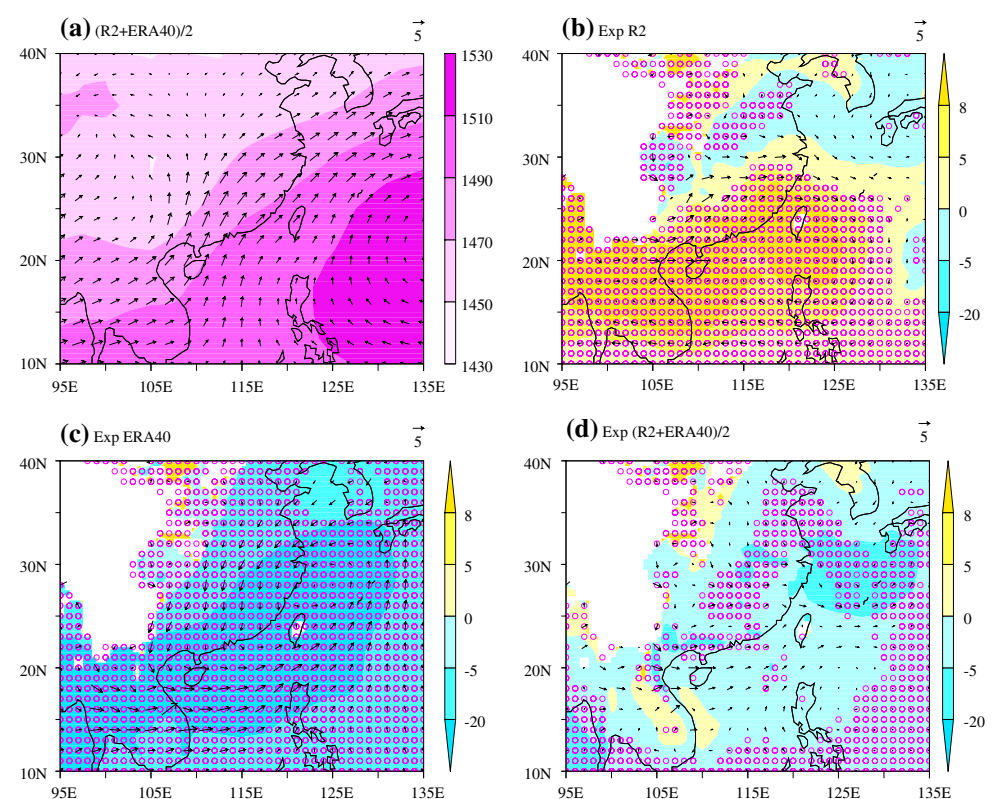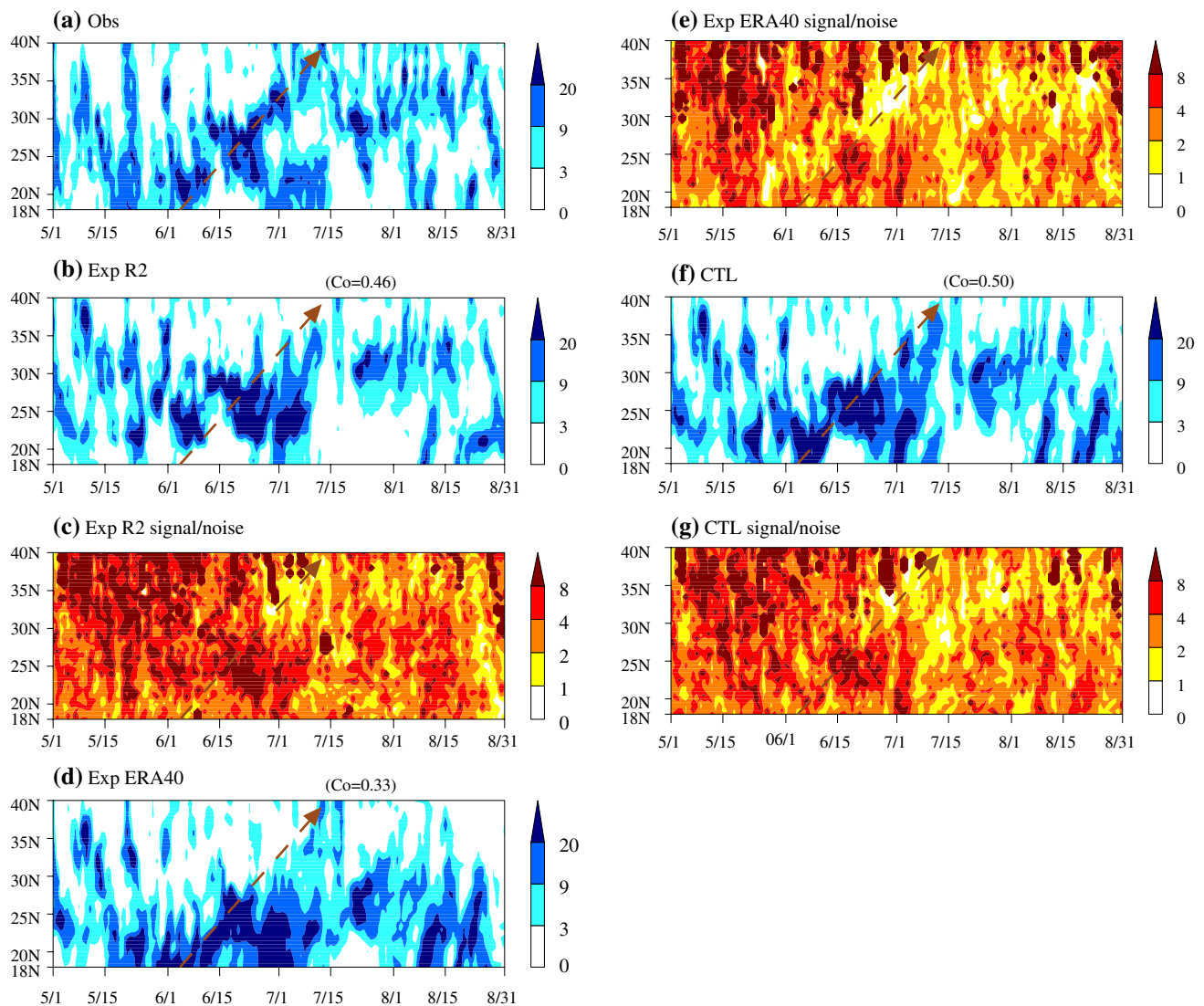
Fig. 3 Time-latitude cross-section of daily precipitation rate (mm day^{-1}) in eastern China averaged between 105 and 122°E from May 1 to August 31, 1998, which were derived from **a** observation, **b** Exp R2, **d** Exp ERA40 and **f** the *CTL* experiment. The observation was based on Chinese rain gauge data from the land area (see Fig. 1 for the gauge locations) and GPCP data over the sea and Taiwan. The thick *dashed arrows* indicate the observed northward march of the rain band. The pattern correlation coefficients between observation and each of the ensemble simulations are indicated in the *upper right corner* of **b**, **d** and **f**. **c**, **e** and **g** are the signal-to-noise ratio of the ensemble experiments for Exp R2, Exp ERA40 and the CTL experiments, respectively

3.2 Remarkable differences in the water vapor fluxes across the lateral boundaries between the two reanalysis datasets

What causes the different biases in the two experiments? Since the WRF model configuration and parameter values were kept the same in all experiments, the major cause must be rooted in the LB forcing fields because the impact of the initial conditions decays with time, while the differences in the boundary conditions retain a persistent influence throughout the season. The boundary forcing fields consist of air temperature, humidity, geopotential height, and winds. We have compared the two reanalysis datasets for each of the above fields. It was found that the differences between the two reanalysis datasets in the temperature, geopotential height, and winds are generally small. However, large differences exist in the humidity fields.

Figure 4 compares the JJA mean vertical profiles of moisture flux (positive toward north and east) computed from the two reanalysis datasets. Along with Fig. 4, we present in Fig. 5 the JJA mean vertically integrated moisture influxes from the surface to 300 hPa across three lateral boundaries; the moisture influx across the northern boundary at 45°N was not shown because it is negligibly small compared to those at the other three lateral

boundaries. At the western boundary (90°E), large moisture flux differences in the vertical direction are seen below 800 hPa (Fig. 4a). As shown in Fig. 5, the differences in meridional direction primarily occur south of the Tibetan Plateau (south of 25°N) over the Bay of Bengal. The total moisture transport across the southern part of the western boundary of the East Asian region in the ERA40 reanalysis is about 18% higher than that in the R2 reanalysis. The differences at the southern boundary (5°N) are primarily found between 850 and 500 hPa in the free troposphere, not in the boundary layer (Fig. 4b). Due to the decrease of water vapor with height, the differences in the total vertically integrated moisture flux across the southern boundary are only about half of the corresponding difference across the western boundary (Fig. 5). Along the eastern boundary at 140°E, the water vapor flux is negative (Fig. 4c), implying a westward transport of water vapor into the model domain. The differences between the two reanalysis datasets in the moisture flux at the eastern boundary are very large below 700 hPa (Fig. 4c). The large discrepancies in the eastern boundary are found mainly over the Philippine Sea from 5 to 20°N, where southeasterly flow prevails on the southern flank of the WNP subtropical ridge (Fig. 5). This westward transport is largely compensated by the eastward transport north of the WNP subtropical ridge located at 20°N, but the net transport across the eastern boundary remains westward (inward). The uncertainties on the eastern boundary are the largest among all four boundaries, reflecting the huge inconsistencies in the two reanalysis data over the WNP, where the observations are very sparse.

Note that the water vapor convergence into the model domain per unit area is 7.99 g m^{-2} s^{-1} in R2 and 11.75 g m^{-2} s^{-1} in ERA40 (Fig. 5). The water vapor convergence in the ERA40 reanalysis is about 47% higher than that of R2, on average. This huge difference was unexpected. It results from the discrepancies in the humidity field as well as the discrepancies in the large-scale divergent winds. The results in Fig. 5 indicate that the largest differences in the total moisture influx are over the Philippine Sea and the Bay of Bengal. The former is associated with the easterly trade winds from the tropical North Pacific, while the latter is associated with the southwest
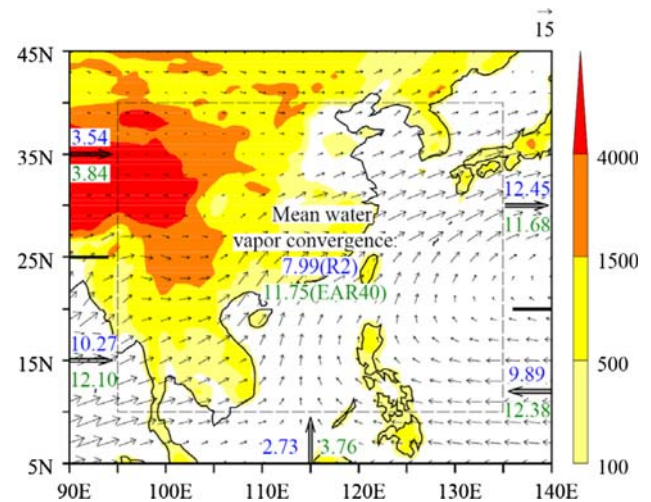

Fig. 5 Summer (*JJA*) mean total vertical integrated water vapor flux (in units of g m^{-2} s^{-1}) through the various segments of the lateral boundaries. The numbers in the center of the domain indicate the JJA mean domain averaged total water vapor convergence per unit area. The *values marked in blue* are derived from R2, while the values marked in green are derived from ERA40. The *double arrows* indicate the direction of water vapor transport. The *arrows* in the model domain represent the JJA mean total vertical integrated water vapor transport vectors derived from the ensemble mean of R2 and ERA40 with unit of 15 g m^{-2} s^{-1}. Topography is shaded according to units of meters. The *dashed box* indicates the inner domain. The area between the lateral boundaries and the dashed box indicates the buffer zone

Indian summer monsoon. The moisture transport from the Bay of Bengal is known as the major channel of water vapor transport to the EASM (Zhou and Yu 2005). The results shown in Fig. 5 suggest that the water vapor transport from the tropical North Pacific is also a major water vapor source. The role of the water vapor transport from the tropical Pacific deserves more attention. In summary, the two reanalysis data show marked discrepancies in the moisture transport in the tropical monsoon regions, particularly over the Bay of Bengal and the Philippine Sea.

The moisture influx over the Plateau and the associated eastward movement of the Plateau weather disturbances can have considerable impacts on the downstream precipitation along the subtropical monsoon front (Wang and Orlanski 1987). Fortunately, the differential moisture influx across the northern portion of the western boundary over

Fig. 4 The JJA mean vertical profiles of moisture fluxes from the surface up to 300 mb averaged along the **a** western, **b** southern, and **c** eastern lateral boundaries. The *dashed lines* indicate results obtained from R2; *solid lines* denote results from ERA40
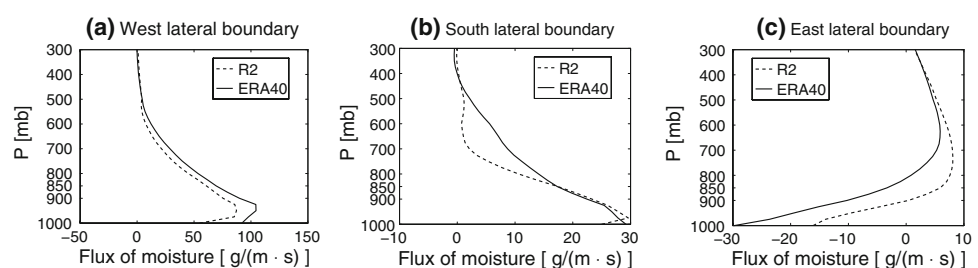
the Tibetan Plateau is relatively small (Fig. 5), which agrees with the findings obtained by Qian et al. (2004).

3.3 Origin of the biases

The large uncertainties in the water vapor flux into the East Asian monsoon domain are believed to be responsible for the differences in the systematic biases seen in Figs. 2 and 3. This assertion was supported by our additional sensitivity experiments. In one such experiment, the LB and initial conditions were the same as those used in Exp ERA40, except that the humidity field was replaced by that derived from R2. The results show that the large cyclonic bias that originally occurred in the Exp ERA40 experiment (Fig. 2c) was drastically reduced (for brevity figure not shown), suggesting that removing the excessive moisture influx from ERA40 indeed effectively corrects the systematic bias in the results of Exp ERA40. The differences in other fields, however, are also partially responsible for the differences in the systematic biases, but they play a minor role.

How can the uncertainties in the LB moisture influx result in circulation biases, such as those seen in Fig. 2? Although the winds and temperature are similar between R2 and ERA40, the large differences between the humidity fields have caused considerable differences in the location and strength of the rainfall or equivalently the atmospheric latent heating, which in turn significantly modified the large scale circulation. This points to the difficulty in downscaling summer climate in East Asia, as atmospheric latent heating is a dominant forcing that drives large scale circulation. The results also suggest, the dynamical LB forcing is weak compared to the atmospheric latent heating in constraining the circulation in the inner domain. Hence downscaling skill is strongly dependent on model physics and boundary forcing (mainly water vapor), both of which affect latent heating.

4 Possible reduction of bias by using ensemble mean LB forcing

Obviously, we do not know which reanalysis product is better than the other in representing nature. Given the uncertainties in the large-scale forcing fields, is there any way to reduce the impacts of the uncertainties on the simulated regional climate? We argue that the physical parameterization schemes used in the models producing R2 and ERA40 are different. We assume that the systematic errors obtained from relatively independent model parameterizations are random. Thus, an ensemble mean of two or more reanalysis datasets would potentially reduce the uncertainties by cancelling out random errors. Uncertainty

arising from model parameterizations is also one of the major sources of errors in dynamic seasonal prediction. To alleviate prediction errors arising from model physical parameterization, the multi-model ensemble (MME) climate prediction has been developed (e.g., Krishnamurti et al. 1999). The idea behind the MME is the promise that if the model parameterizations are independent of each other, the uncertainty-induced errors in each model may be random in nature; thus, an average approach may reduce the prediction errors induced by the model parameterization schemes. It has been demonstrated that the MME prediction performs better than any single-model component (e.g., Palmer et al. 2000; Shukla et al. 2000; Wang et al. 2004a).

Drawing upon the aforementioned hypothesis, a control (CTL) run, which was an ensemble mean of five members, was conducted with the same initial times as used in Exp ERA40 or Exp R2, In the CTL experiment the ensemble mean ERA40 and R2 was used as the driving data for the WRF model. The simulated biases of JJA mean height and low-level circulation in the CTL experiment, shown in Fig. 2d, indeed yielded improved low-level circulations. The errors in simulated geopotential height field are much smaller and the winds do not show an organized pattern compared to those using individual ERA40 and R2 reanalysis products as the driving data.

The improvement is also seen in individual monthly mean fields and seasonal evolution (Fig. 3f). As shown in Fig. 3f, the CTL may better simulate the seasonal march of the East Asian monsoon rain band than those in both the Exp R2 and Exp ERA40. The correlation coefficient between CTL and observation is 0.50, while that between R2 and observation is 0.46, and that between ERA40 and observation is 0.33.

The observed EASM rainy season in 1998 exhibits three distinct stages. The first stage is from May 15 to the end of May 31. A sudden increase in rainfall around May 20 signifies the onset of the South China Sea summer monsoon (Wang et al. 2004b). In late May and early June, the major rain band remains between 18 and 24°N (Fig. 3a). The second stage of the rainy season is characterized by a systematic northward migration of the monsoon rain band from early June to mid-July, as highlighted by the arrow in Fig. 3a. Neither the R2 nor ERA40 simulation reproduces this seasonal march realistically (Figs. 3b, d). However, the CTL simulation may capture better this seasonal march (Fig. 3f). The third stage of the rainy season lasts from July 15 to August 5. Notable features are the sudden southward retreat of the East Asian monsoon rain band around July 16, and the subsequent return of heavy rains in the Yangtze River basin between 26 and 33°N (Fig. 3a). These peculiar features were captured reasonably well by the CTL experiment (Fig. 3f); and again, the simulations in Exp R2

Fig. 6 The observed (*solid*) and simulated (CTL, *dash-dotted*) area-averaged daily precipitation rates (mm/day) from May 1 to August 31, 1998, over the land area of the following three regions: **a** North China, **b** the Yangtze River basin, and **c** South China (see Fig. 1 for definition). The correlation coefficients are indicated in the *top right corner* of each panel. The *shadings* show the spreading and the envelopes of the ensemble members
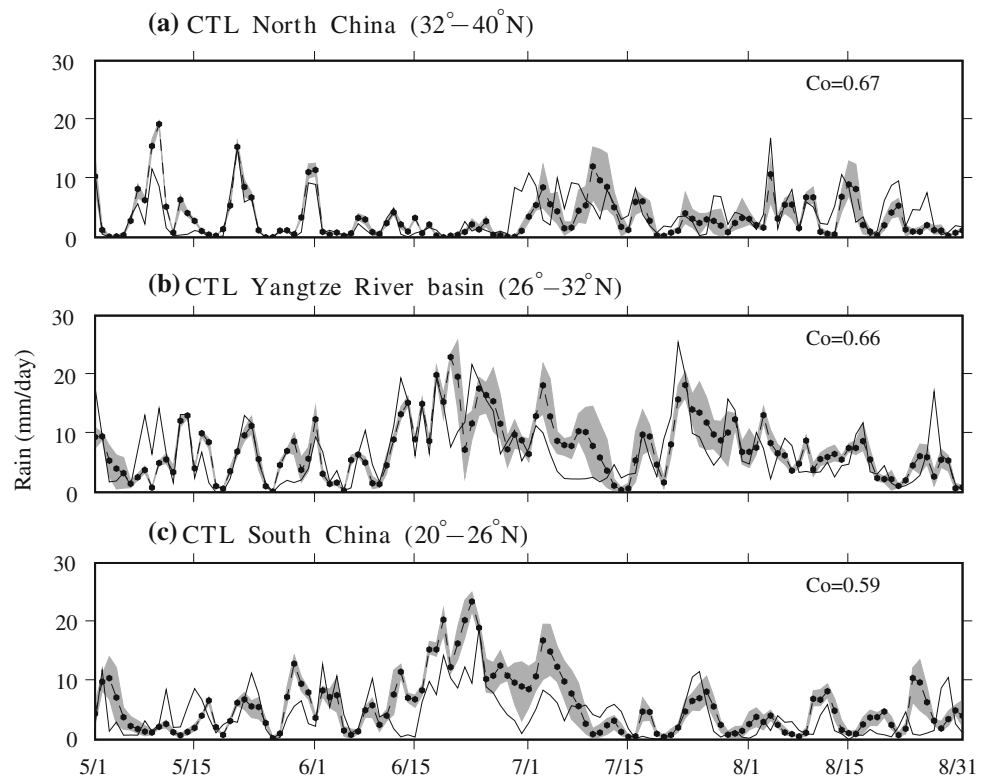
and Exp ERA40 show seemingly larger biases than in the CTL simulation.

The inter-member spreading has been computed to quantify the model's internal variability and to provide a measure of the robustness of the results. In Fig. 3c, e, and g, the signal to noise ratio, i.e., the ratio of the ensemble mean to the inter-member standard deviation, is shown. The large values of the signal-to-noise ratio suggest that uncertainties induced by different initial conditions are very low, thus, the results are robust.

What about the simulation of individual precipitation events? Figure 6 presents the time series of daily precipitation rates averaged over three land areas in North China, the Yangtze River basin, and South China (see Fig. 1 for their locations). The results obtained from the CTL experiment were compared with the rain gauge observations. The CTL experiment closely reproduces individual precipitation events. The correlation coefficients between the observed and simulated time series are 0.67, 0.66, and 0.59, respectively, in North China, the Yangtze River basin, and South China (Fig. 6; Table 1). Thus, on average, the correlation coefficient between observation and CTL simulation is 0.64. This performance is possibly better, since the correlation score obtained in Exp R2 is 0.58 and 0.52 in Exp ERA40. Table 1 shows also the signal-to-noise ratio associated with the three regional precipitation time series in order to measure the robustness of the results. For example, over North China in Exp ERA40, we have five time series

from the areal averaged rainfall from the five ensemble members, i.e., X_{ti}, $t = 1,\ldots,123$, $i = 1,\ldots,5$. From the five time series, we get the time series of signal-to-noise ratio, $Y_t = \text{mean}(X_{ti})/\text{std}(X_{ti})$. Then this time series of signal-to-noise ratio is averaged over the entire period of simulation, i.e., $Z = \text{mean}(Y_t)$. The Z values shown in Table 1 indicate that the uncertainties arising from the internal dynamics is small and the ensemble means are robust.

Of note is that the two heavy rain periods over the Yangtze River valley, occurring in mid-late June (enhanced normal Meiyu) and in mid-late July (the abnormal return of Meiyu), are captured reasonably well, although the discrepancy is relatively large in early July (Fig. 6b). In addition, the time series of the corresponding standard deviation was calculated with respect to the regional mean daily precipitation. The values of the area mean standard

Table 1 Temporal correlation coefficients (italic values) between the observed and simulated area mean daily precipitation rate (mm/day) from May 1 to August 31, 1998, over North China, the Yangtze River basin, and South China (see Fig. 1 for locations of the three regions). Shown are also the corresponding signal-to-noise ratios among the ensemble members (roman values)

Correlation Signal/noise	Exp R2		Exp ERA40		CTL	
North China	*0.62*	8.77	*0.54*	6.09	*0.67*	7.06
Yangtze River basin	*0.55*	12.28	*0.58*	5.17	*0.66*	8.80
South China	*0.56*	8.71	*0.43*	4.59	*0.59*	6.19

deviation in each region describe the amplitude of the spatial variability of daily precipitation. The simulated variability in the CTL matches the observations very well (figure not shown). The results shown in Figs. 3 and 6 indicate that with the ensemble mean LB condition the WRF model reproduces not only improved seasonal mean precipitation and circulation (Fig. 2d), but also possibly improved sub-seasonal variability and individual heavy rainfall events in the East Asian region.

5 Water vapor budget

Given a large-scale LB forcing, an RCM with suitably high-resolution that resolves complex orography, land-sea contrast and land-surface properties is expected to generate improved high-resolution information that is coherent with the large-scale driving circulation. When an RCM is nested in a global domain, the global domain with a coarser mesh provides boundary conditions to the finer-mesh RCM. A common practice is to use a buffer zone inside the LB to pass large-scale forcing to regional atmospheric motion. The buffer zone is a transitional region in which the inner solution is gradually "nudged" to match the large-scale LB conditions. In the present model, the buffer zone consists of 10 grids over which the weighting function allows large-scale LB values to decrease linearly to zero.

The atmospheric branch of the hydrological cycle can be described by the following water vapor budget equation (e.g., Peixoto and Oort 1992):

$$\frac{\partial W}{\partial t} + \nabla \cdot Q = E - P, \tag{1}$$

where $W \equiv (1/g) \int_0^{p_s} q \, dp$, $Q \equiv (1/g) \int_0^{p_s} V q \, dp$, E, P, g, q, p, p_s, and V are precipitable water, moisture flux, evaporation, precipitation, gravity, specific humidity, pressure, surface pressure, and the horizontal velocity vector, respectively. In the WRF model, q includes six components: vapor, ice, snow, cloud, rain water, and graupel. Computation of Q requires special care. When Q is calculated with our diagnostic grid, significant errors will result, due to interpolation of the model grid to the diagnostic grid (Trenberth 1991), especially over the complex terrain. To avoid this type of error, we calculated Q in σ coordinates, i.e., $Q = [(p_s - p_t)/g] \int_0^1 V q \, d\sigma$, where p_t is the pressure at the top of the model. With this treatment, the error caused by the difference in discretization between the model and the diagnostic grids is negligibly small.

The budget Eq. 1 is a mathematical description of water vapor conservation. Integration of Eq. 1 over a specific domain and then taking a domain average yield

$$MC = Pr - Ev + dW \tag{2}$$

where all terms in (2) are domain-averaged quantities per unit area; MC denotes the amount of water vapor per unit area that enters the specific domain through the lateral boundaries; Pr and Ev represent, respectively, the precipitation and the surface evaporation rate; and dW is time rate of change of precipitable water. Equation 2 states that the total amount of water vapor that enters a specific domain must be balanced by the sum of the precipitation, minus evaporation, and the increase in precipitable water storage.

Computation of the water vapor budget in the ensemble mean large-scale forcing field shows that over the entire regional domain, the water vapor is not conserved. As shown in Fig. 7a, the water vapor converging into the domain in the large scale forcing fields (denoted by MC$_{LBF}$) noticeably differs from the residual term on the right-hand side of the Eq. 2, i.e., the sum of the total amount of precipitation and the increase in water vapor storage minus evaporation (denoted by MC$_{RES}$). Of interest is that the MC$_{LBF}$ peaks in June, but the precipitation peaks in July. This type of imbalance in water vapor budget is seen in the two original reanalysis datasets. The reasons have been discussed by Roads et al. (2002). Given this imbalanced large-scale water vapor forcing, it is interesting to see what happens in the regional model simulation.

Analysis of the water vapor budget in the CTL run over the entire RCM model domain indicates that the water vapor converging into the domain provided by the large-scale boundary conditions also differs from the residual term computed from the WRF CTL experiment (figure not shown). However, the imbalance occurs only in the buffer zone. Figure 7b and c show the monthly mean water vapor budget within the inner domain and the buffer zone, respectively. On the monthly time scale, the water vapor converging into the inner domain (inside the buffer zone) is approximately balanced by the precipitation minus the surface evaporation (Fig. 7b). The monthly change of the precipitable water (dW) is negligibly small compared to the other three terms in Eq. 2: the increase in atmospheric precipitable water in May and June and the decrease in July and August have a tiny magnitude on an order of 0.1 mm day^{-1}. On the other hand, in the buffer zone, as shown in Fig. 7c, the total amount of water vapor that goes into the domain through lateral boundaries, denoted by MC$_{LBF}$, is remarkably different from the residual moisture convergence MC$_{RES}$. In the buffer zone, the relative error in the water vapor convergence, which is measured by

$$e = (MC_{RES} - MC_{LBF})/MC_{LBF} \times 100\%,$$

is -135.0% in May, $+62.3\%$ in June, -37.9% in July, and -50.8% in August. A negative value of e means a moisture "loss" in the buffer zone. During the entire summer (May through August), about 45.0% of total water vapor
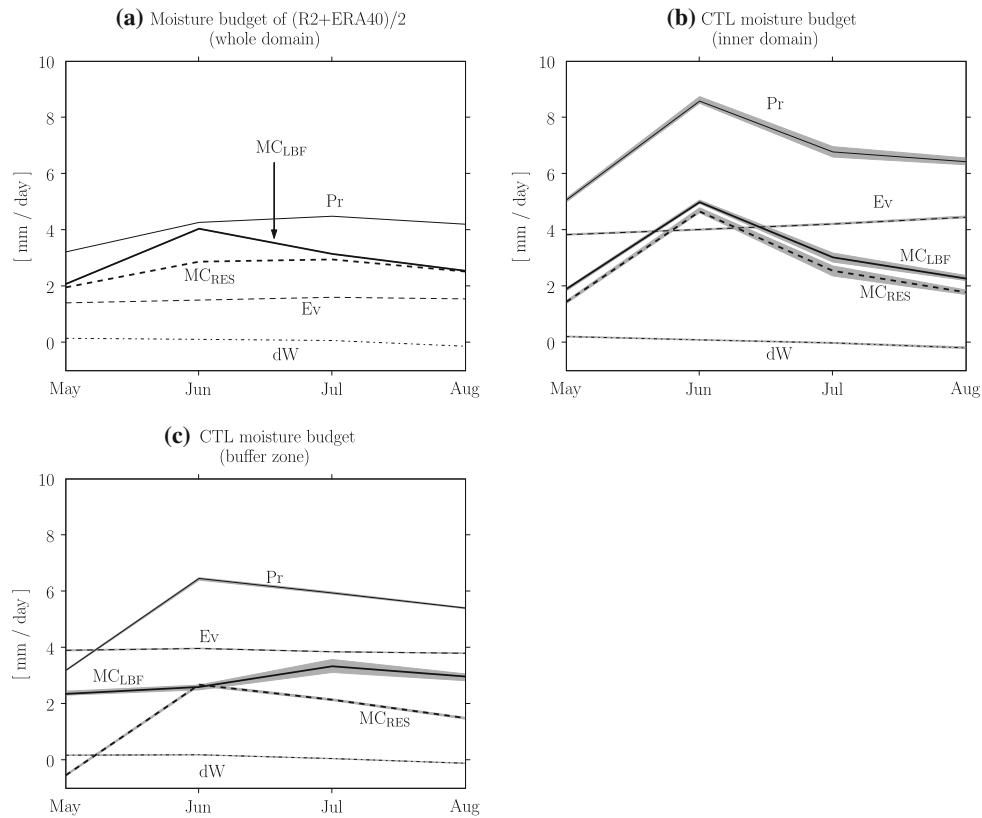
Fig. 7 Monthly mean moisture budget analysis in **a** the large-scale driving data, i.e., the ensemble mean of the R2 and ERA40 reanalysis data over the whole domain (5–45°N and 90–140°E) and **b** the WRF model control (*CTL*) experiment over the inner domain (10–40°N and 95–135°E). **c** is the same as in (**b**) except for the buffer zone. The notations MC$_{LBF}$, Pr, Ev, d*W*, and MC$_{RES}$ represent, respectively, the moisture convergence across the lateral boundaries into the domain; precipitation; surface evaporation; the time rate of change of the atmospheric precipitable water; and the residual moisture convergence, i.e., the precipitation minus the sum of the evaporation and the decrease in moisture storage. All components denote the rate per unit area (mm day^{-1}) averaged over the specified domain. The *shadings* denote the spreading and envelopes of the ensemble members in the control run

entering the buffer zone is lost there. We conjecture that the water vapor deficit in the buffer zone is primarily induced by the effects of the artificial "nudging." In addition, the difference in representation of orography between the large-scale forcing and the WRF model, especially at the western boundary that is located over the Tibetan plateau, could also contribute to the water vapor imbalance. The original large-scale forcing from reanalysis does not warrant moisture conservation. But, in the inner domain the regional model simulation observes water vapor conservation.

Of interest is that the CTL solution not only corrects the imbalance in water vapor budget, it also corrects the errors in the sub-seasonal evolution of the large-scale precipitation and improves the accuracy in predicting total amount of precipitation. Over eastern China, including North China, the Yangtze River basin and South China, the station rain gauge data and the CMAP and GPCP data all show maximum monthly precipitation occurring in June 1998 (Fig. 8). This maximum coincides with the period of

Yangtze River overflow. The maximum rainfall in the ensemble R2 and ERA40, however, erroneously occurred in July. The WRF model CTL experiment, on the other hand, correctly determines the maximum in June. In general, the simulated changes of the total precipitation from month to month in the CTL experiments agree well with observations, except for a slight overestimate of rainfall in May, June, and July (Fig. 8). Compared to the original large-scale precipitation (ensemble mean of R2 and ERA40), the WRF model simulation provides a more realistic precipitation amount.

In the above we have stressed the added values of the RCM in correcting hydrological biases of the forcing field on the monthly mean time scale (Figs. 7, 8). However, that is not to say that when the RCM is driven by reanalysis fields, its simulated precipitation variability on daily time scale would also be better than reanalysis. In fact, we have examined the seasonal march (similar to Fig. 3) and area mean daily precipitation (similar to Fig. 6) in the two reanalysis datasets. The results show that the RCM

Domain averaged monthly rainfall rate on land
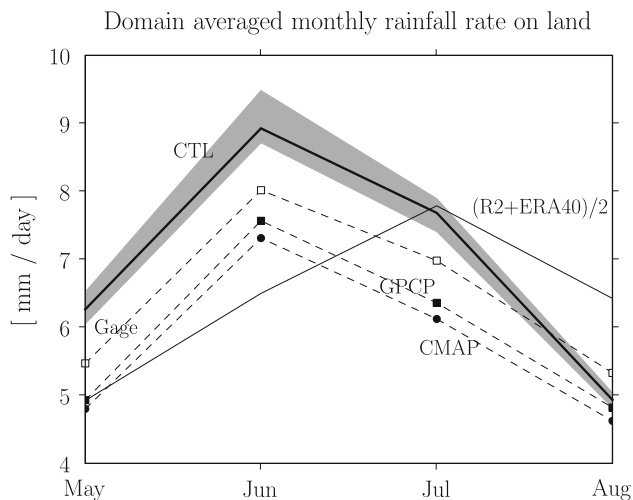
Fig. 8 Comparison of the area-averaged monthly mean precipitation rates in the land area in East China (20–40°N, 105–122°E) obtained from the CTL run with those obtained from the large-scale forcing (i.e., ensemble mean of the R2 and ERA40 reanalysis data), Chinese rain gauge data, and the CMAP and GPCP datasets. The shaded area indicates the spreading and envelopes of the ensemble members in the control run

simulations are considerably worse than the counterparts in the reanalysis. The reason is that Fig. 3 and Fig. 6 reflects precipitation variation on the daily time scale. Keep in mind that while precipitation itself is not constrained in the reanalysis, other fields (winds, pressure, temperature and humidity) which leads to precipitation fields are constrained by observations on twice daily basis, thus daily precipitation variability in reanalysis dataset tends to resemble observation. In the RCM, on the other hand, none of the above mentioned fields inside of the domain are constrained by observation, thus the daily precipitation variability is to large extent determined by RCM internal dynamics. Therefore, it is expected that on the daily time scale the reanalysis should outperform the RCM. Keep also in mind that when a RCM is used for regional downscaling or future projection, the lateral forcing for RCM will come from global model forecast. In that case, both global and regional model results are not constrained by observation and the RCM could outperform the global models.

6 Summary

This article examines the hydroclimate aspects of regional climate modeling, especially the uncertainties in the LB moisture flux forcing and the humidity transfer between reanalysis or global models and the RCM. We have shown that, for the same WRF model setting, the simulations of the 1998 summer monsoon yielded large discrepancies when different LB forcing data were used to drive the WRF

model. The boundary conditions derived from the widely used National Centers for Environmental Prediction/Department of Energy Reanalysis-2 (R2) and the European Centre for Medium-Range Weather Forecasts 40-Year Reanalysis (ERA40) have been considered to be the best available surrogates to observations. Therefore, the remarkable differences in the regional model simulations forced by the two reanalysis datasets are unexpected and, to the authors' knowledge, have not been reported before in the simulation of the EASM, although the sensitivity of the RCM solutions to large-scale LB forcing is well known.

We have demonstrated that the differences in the simulation results are caused by uncertainties in the moisture influx at the lateral boundaries, whereas uncertainties in circulation and air temperature have minor impacts. One of the surprising results is that the summer-mean water vapor convergence into the model domain computed from the ERA40 is 47% higher than that computed from the R2 reanalysis. The largest uncertainties in the moisture transport across the LB are found over the Philippine Sea and the Bay of Bengal. The water vapor transport from the Bay of Bengal to the EASM region is well recognized as a major source of water vapor in the EASM. But, the importance of the water vapor transport from the tropical North Pacific has been less emphasized.

The results in the model simulation forced by the ensemble mean LB conditions reproduce not only improved seasonal mean precipitation and circulation (Fig. 2) but also possible improvement in sub-seasonal variability (Fig. 3) and individual heavy rainfall events in the East Asian region (Fig. 6). It is suggested that the simulation errors may be reduced by using an "ensemble" average of two or more reanalysis datasets as LB forcing. This finding is interesting but its validity requires further verification by using multi-models and by performing long-period experiments.

The potential advantages of using ensemble forcing are based on the following consideration. The physical parameterization schemes used in the models producing R2 and ERA40 are different. We assume that the systematic errors obtained from relatively independent model physics are random, thus, ensemble average can generally reduce errors relative to each individual reanalysis dataset. We have further examined the solution driven by global energy and water experiment (GEWEX) Asian monsoon experiment (GAME) reanalysis. The characteristics found here remain valid.

The regional model simulation was shown to be able to correct a number of biases in the original large-scale hydrological cycle. The water vapor is not conserved in the large-scale forcing field. However, with such a large-scale forcing, the regional model solution conserves water vapor in the interior domain, confining the imbalance to the

boundary buffer zone. Further, compared to large-scale driving fields, the total amount of precipitation in the regional model is increased and in much better agreement with observations. The original large-scale precipitation in the driving data shows an erroneous maximum rainfall in July, but the regional model solution shows the correct peak, which occurred in June 1998. In spite of the added values that RCM has in improving water cycle on monthly mean time scale, the daily precipitation simulated by RCM is far below the reanalysis. The reason is that the winds, pressure, temperature and humidity fields which lead to precipitation fields are constrained by observations on twice daily basis, while in the RCM none of the above-mentioned fields inside of the domain are constrained by observation and daily precipitation variability is to large extent determined by RCM internal dynamics.

In a previous study (Wang et al. 2003), a regional model, IPRC RegCM, driven by ERA40, yielded better results than a model driven by R2 data. In the present study, the WRF model simulation with R2 forcing is seemingly more accurate than the simulation driven by the ERA40 data. The reason is likely due to the fact that the WRF model physics is close to the NCEP model that was used to produce the R-2 data. Similarly, the cumulus parameterization scheme in IPRC RegCM is very close to that in ECMWF model.

The soil moisture initial conditions in experiments ERA40 and R2 are different. To see whether this will affect our conclusion regarding the effects of LB moisture fluxes, we performed an extra experiment with ERA40 as the LBC, but the initial soil moisture is provided by R2. The results show that initial soil moisture anomaly didn't change our conclusions qualitatively. The reason is that for the summer monsoon the soil moisture-precipitation feedback appears to be less important than the moisture flux convergence anomaly, although soil moisture memory could act as low frequency forcing to the land-atmospheric system. Our results showed that variability in evaporation rate is relatively small and the change of precipitation is highly coherent with the change of moisture flux convergence.

The results reported here have important ramifications for validation of RCMs. The errors in regional modeling results come from the uncertainties in both the model's physical parameterizations and the LB conditions. This mixed source poses a challenge for validation of the physics in the regional model. This study has shown that the RCM solutions can be considerably different if different reanalysis forcing is used. Previous regional model intercomparison projects took a single set of the reanalysis as lateral forcing field to assess the degree of success of the models. Given the large uncertainties in the reanalysis data, one should realize that the conclusions made from

such comparison may be changed if another set of reanalysis is used as LB forcing. This finding calls for cautions in our methodology for verification of the RCMs and calls for attention to reshape our strategy for validation models.

In the EASM region, the primary boundary uncertainties are found in the water vapor transport from the ocean. Accurate observations over the Bay of Bengal, the South China Sea, and the western North Pacific are critical for improving regional modeling of the EASM. These places are in need of improved observations. With the launch of A-Train satellites, the access to three-dimensional measurements of moisture and temperature fields over the ocean is expected to lessen the uncertainties in the LB forcing in RCM simulations. It would be interesting to see the impacts of satellite observations on the quality of future reanalysis products. For downscaling global prediction and projections for the EASM region, the same hydrological issue would pose a great challenge.

Our numerical experiments are based on only one model ensemble simulation of summer 1998. Decadal simulations (Jones et al. 1995) with multiple models are needed to validate the robustness of the conclusions obtained here. Nevertheless, the issues addressed here may provide useful insight for future design of RCM intercomparison project.

References

Anderson CJ, Arritt RW, Takle ES, Pan Z, Gutowski WJ, Otieno FO, Silva RD, Caya D, Christensen JH, Lüthi D, Gaertner MA, Gallardo C, Giorgi F, Hong S-Y, Jones C, Juang H-M, Katzfey JJ, Lapenta WM, Laprise R, Larson JW, Liston GE, McGregor JL, Pielke RA, Roads JO, Taylor JA (2003) Hydrologic processes in regional climate model simulations of the central United States flood of June-July 1993. J Hydrometeor 4:584–598

Beniston M, Stephenson D, Christensen O, Ferro C, Frei C, Goyette S, Halsnaes K, Holt T, Jylhae K, Koffi B, Palutikof J, Schoell R, Semmler T, Woth K (2007) Future extreme events in European climate: an exploration of regional climate model projections. Clim Change 81(s1):71

Bhaskaran B, Jones RG, Murphy JM, Noguer M (1996) Simulations of the Indian summer monsoon using a nested regional climate model: Domain size experiments. Climate Dyn 12:573–587

Chen F, Dudhia J (2001) Coupling an advanced land surface-hydrology model with the Penn State-NCAR MM5 modeling system. Part I: model implementation and sensitivity. Mon Wea Rev 129:569–585

Chen S-H, Sun W-Y (2002) A one-dimensional time dependent cloud model. J Meteor Soc Jpn 80:99–118

Chen T-C (2006) Variation of the Asian monsoon water vapor budget: Interaction with the global-scale modes. In: Wang B (ed) The Asian monsoon. Springer, Berlin, pp 417–457

Christensen JH, Machenhauer B, Jones RG, Schar C, Ruti PM, Castro M, Visconti G (1997) Validation of present-day regional climate simulations over Europe: LAM simulations with observed boundary conditions. Climate Dyn 13:489–506

Curry JA, Lynch AH (2002) Comparing arctic regional climate models. Eos Trans Am Geophys Union 83:87

Denis B, Laprise R, Caya D, Coté J (2002) Downscaling ability of one-way nested regional climate models: the Big-Brother Experiment. Climate Dyn 18:627–646

Ding Y, Liu Y (2001) Onset and the evolution of the summer monsoon over the South China Sea during SCSMEX field experiment in 1998. J Meteor Soc Jpn 79:255–276

Ding Y, Sikka DR (2006) Synoptic systems and weather. In: Wang B (ed) The asian monsoon. Springer, Berlin, pp 131–202

Dudhia J (1989) Numerical study of convection observed during the winter monsoon experiment using a mesoscale two-dimensional model. J Atmos Sci 46:3077–3107

Fasullo J, Webster PJ (2002) Hydrological signatures relating the Asian summer monsoon and ENSO. J Clim 15:3082–3095

Fu C, Wang S, Zhe X, Gutowski WJ, Lee D-K, McGregor JL, Sato Y, Kato H, Kim J-W, Suh M-S (2005) Regional climate model intercomparison project for Asia. Bull Am Meteor Soc 86:257–266

Giorgi F, Bi X (2000) A study of internal variability of a regional climate model. J Geophys Res 105:29503–29521

Giorgi F, Mearns LO (1999) Introduction to special section: regional climate modeling revisited. J Geophys Res 104:6335–6352

Hong S-Y, Leetmaa A (1999) An evaluation of the NCEP RSM for regional climate modeling. J Clim 12:592–609

Huffman GJ, Adler RF, Morrissey MM, Bolvin DT, Curtis S, Joyce R, McGavock B, Susskind J (2001) Global precipitation at one-degree daily resolution from multiSatellite observations. J Hydrometeor 2:36–50

Jacob D, Podzun R (1997) Sensitivity studies with the regional climate model REMO. Meteor Atmos Phys 63:119–129

Janjic ZI (2000) Comments on "Development and evaluation of a convection scheme for use in climate models". J Atmos Sci 57:3686

Jones RG, Murphy JM, Noguer M (1995) Simulation of climate change over Europe using a nested regional-climate model. Part I: assessment of control climate, including sensitivity to location of boundaries. Q J R Meteor Soc 121:1413–1449

Kanamitsu M, Ebisuzaki W, Woollen J, Yang S-K, Hnilo JJ, Fiorino M, Potter GL (2002) NCEP-DOE AMIP-II Reanalysis (R-2). Bull Am Meteor Soc 83:1631–1643

Krishnamurti TN, Bhalme HN (1976) Oscillations of monsoon system. Part I: observational aspects. J Atmos Sci 33:1937–1954

Krishnamurti TN, Kishtawal CM, Zhang Z, LaRow TE, Bachiochi DR, co-authors (1999) Improved weather and seasonal climate forecasts from multi-model superensemble. Science 285:1548–1550

Leung LR, Ghan SJ (1999) Pacific Northwest climate sensitivity simulated by a regional climate model driven by a GCM. Part I: control simulations. J Clim 12:2010–2030

Liang X-Z, Kunkel KE, Samel AN (2001) Development of a regional climate model for US midwest applications. Part I—sensitivity to buffer zone treatment. J Clim 14:4363–4378

Liang X-Z, Li L, Kunkel KE, Ting M, Wang JX (2004) Regional climate model simulation of US precipitation during 1982–2002. Part I: annual cycle. J Clim 17:3510–3529

Lin Y-L, Farley RD, Orville HD (1983) Bulk parameterization of the snow field in a cloud model. J Clim Appl Meteor 22:1065–1092

Miyakoda K, Rosati A (1977) One way nested grid models: The interface conditions and the numerical accuracy. Mon Wea Rev 105:1092–1107

Noh Y, Cheon WG, Hong SY, Raasch S (2003) Improvement of the K-profile model for the planetary boundary layer based on large eddy simulation data. Bound Layer Meteor 107:401–427

Paegle J, Yang Q, Wang M (1997) Predictability in limited area and global models. Meteor Atmos Phys 63:53–69

Palmer TN, Brankovic C, Richardson DS (2000) A probability and decision-model analysis of PROBOST seasonal multi-model ensemble integrations. Q J R Meteorol Soc 126:2013–2034

Pan Z, Christensen JH, Arritt RW, Gutowski Jr WJ, Takle ES, Otieno F (2001) Evaluation of uncertainties in regional climate change simulations. J Geophys Res 106:17735–17751

Peixoto JP, Oort AH(1992) Physics of climate. American Institute of Physics, pp 520

Qian J-H, Tao W-K, Lau K-M (2004) Mechanisms for torrential rain associated with the Mei-Yu development during SCSMEX 1998. Mon Wea Rev 132:3–27

Roads J, Kanamitsu M, Stewart R (2002) CSE water and energy budgets in the NCEP–DOE reanalysis II. J Hydrometeor 3:227–248

Shukla J, coauthors (2000) Dynamical seasonal prediction. Bull Am Meteor Soc 81:2493–2606

Skamarock WC, Klemp JB, Dudhia J, Gill DO, Barker DM, Wang W, Powers JG(2005) A description of the advanced research WRF version 2. NCAR technical note, NCAR/TN-468+STR

Takle ES, Gutowski WJ, Arritt RW, Pan Z, Anderson CJ, da Silva RR, Caya D, Chen S-C, Giorgi F, Christensen JH, Hong S-Y, Juang H-M, Katzfey J, Lapenta WM, Laprise R, Liston GE, Lopez P, McGregor J, Pielke RA, Roads JO (1999) Project to intercompare regional climate simulations (PIRCS): Description and initial results. J Geophys Res 104:19443–19461

Trenberth KE (1991) Climate diagnostics from global analyses: conservation of mass in ECMWF analyses. J Clim 4:707–722

Uppala SM, Kallberg PW, Simmons AJ, Andrae U, da Costa Bechtold V, Fiorino M, Gibson JK, Haseler J, Hernandez A, Kelly GA, Li X, Onogi K, Saarinen S, Sokka N, Allan RP, Andersson E, Arpe K, Balmaseda MA, Beljaars ACM, van de Berg L, Bidlot J, Bormann N, Caires S, Chevallier F, Dethof A, Dragosavac M, Fisher M, Fuentes M, Hagemann S, HólmE, Hoskins BJ, Isaksen L, Janssen PAEM, Jenne R, McNally AP, Mahfouf J-F, Morcrette J-J, Rayner NA, Saunders RW, Simon P, Sterl A, Trenberth KE, Untch A, Vasiljevic D, Viterbo P, Woollen J (2005) The ERA-40 re-analysis. Q J Roy Meteor Soc 131:2961–3012

Vukicevic T, Errico RM (1990) The influence of artificial and physical factors upon predictability estimates using a complex limited-area model. Mon Wea Rev 118:1460–1482

Wang B, Orlanski I (1987) Study of a heavy rain vortex formed over the eastern flank of the Tibetan Plateau. Mon Wea Rev 115:1370–1393

Wang B, LinHo (2002) Rainy season of the Asian–Pacific summer monsoon. J Clim 15:386–398

Wang B, Kang I-S, Lee J-Y (2004a) Ensemble simulations of Asian–Australian monsoon variability by 11 AGCMs. J Clim 17:803–818

Wang B, LinHo Y, Zhang Y, Lu M-M (2004b) Definition of South China sea monsoon onset and commencement of the East Asia summer monsoon. J Clim 17:699–710

Wang Y, Sen OL, Wang B (2003) A highly resolved regional climate model (IPRC-RegCM) and its simulation of the 1998 severe precipitation event over China. Part I: model description and verification of simulation. J Clim 16:1721–1738

Williams EJ (1959) The comparison of regression variables. J R Stat Soc Ser B 21:396–399

Wu W, Lynch AH, Rivers A (2005) Estimating the uncertainty in a regional climate model related to initial and lateral boundary conditions. J Clim 18:917–933

Xie P, Arkin PA (1997) Global precipitation: a 17-year monthly analysis based on gauge observations, satellite estimates and numerical model outputs. Bull Am Meteor Soc 78:2539–2558

Yasunari T, Miwa T (2006) Convective cloud systems over the Tibetan Plateau and their impact on meso-scale disturbances in the Meiyu/Baiu frontal zone—a case study in 1998. J Meteorol Soc Jpn 84:783–803

Zhong Z (2006) A possible cause of a regional climate model's failure in simulating the east Asian summer monsoon. Geophys Res Lett 33:L24707. doi:10.1029/2006GL027654

Zhou T-J, Yu R-C (2005) Atmospheric water vapor transport associated with typical anomalous summer rainfall patterns in China. J Geophys Res 110:D8 104